Photoexcitation in two-dimensional topological insulators: Generating and controlling electron wavepackets in Quantum Spin Hall systems

(Article begins on next page)

14 October 2024

THE EUROPEAN
PHYSICAL JOURNAL
SPECIAL TOPICS

Regular Article

Photoexcitation in two-dimensional topological insulators

Generating and controlling electron wavepackets in Quantum Spin Hall systems

Fabrizio Dolcini[a] and Fausto Rossi

Dipartimento di Scienza Applicata e Tecnologia, Politecnico di Torino corso Duca degli Abruzzi 24, 10129 Torino, Italy

Abstract. One of the most fascinating challenges in Physics is the realization of an electron-based counterpart of quantum optics, which requires the capability to generate and control single electron wave packets. The edge states of quantum spin Hall (QSH) systems, i.e., two-dimensional (2D) topological insulators realized in HgTe/CdTe and InAs/GaSb quantum wells, may turn the tide in the field, as they do not require the magnetic field that limits the implementations based on quantum Hall effect. However, the band structure of these topological states, described by a massless Dirac fermion Hamiltonian, prevents electron photoexcitation via the customary vertical electric dipole transitions of conventional optoelectronics. So far, proposals to overcome this problem are based on magnetic dipole transitions induced via Zeeman coupling by circularly polarised radiation, and are limited by the g-factor. Alternatively, optical transitions can be induced from the edge states to the bulk states, which are not topologically protected though.

Here we show that an electric pulse, localized in space and/or time and applied at a QSH edge, can photoexcite electron wavepackets by intra-branch electrical transitions, without invoking the bulk states or the Zeeman coupling. Such wavepackets are spin-polarised and propagate in opposite directions, with a density profile that is independent of the initial equilibrium temperature and that does not exhibit dispersion, as a result of the linearity of the spectrum and of the chiral anomaly characterising massless Dirac electrons. We also investigate the photoexcited energy distribution and show how, under appropriate circumstances, minimal excitations (Levitons) are generated. Furthermore, we show that the presence of a Rashba spin–orbit coupling can be exploited to tailor the shape of photoexcited wavepackets. Possible experimental realizations are also discussed.

---

[a] e-mail: fabrizio.dolcini@polito.it

1 Introduction

Electron quantum optics is one of the most fascinating and rapidly growing fields in Physics. Its goal, i.e., the realization of an electron-based counterpart of quantum optics, requires the capability to generate and control single electron wave packets, where one could encode, transmit and process information [1–3]. Presently, the edge channels of quantum Hall (QH) systems are considered the reference platform to achieve this purpose [4–15]: electrons injected by electron pumps in these chiral one-dimensional (1D) edge channels can propagate ballistically and coherently over various micrometers, topologically protected from backscattering off disorder. Furthermore, quantum point contacts can be used as the analogue of electron beam splitters. There is, however, a major drawback limiting the large scale applications of QH-based electron quantum optics, namely the strong values of magnetic field that are needed to generate the ballistic edge states.

A quite promising alternative is the quantum spin Hall (QSH) effect [16–18], where edge channels do not require any applied magnetic field, as they originate from a spin–orbit induced topological transition. These QSH edge channels, observed in HgTe/CdTe [19–22] and InAs/GaSb [23–26] quantum wells, are also protected from backscattering off non-magnetic impurities, as their group velocity is locked to their spin orientation. Notably, QSH edge states also offer two more important advantages. First, quite similarly to photons, they exhibit a linear electronic spectrum, where the Fermi velocity v_F plays the role of the speed of light c. As a consequence, a freely propagating electronic wave packet does not feature the customary dispersion arising in conventional parabolic band materials. This is crucial for the information transmission rate, which requires the generation of wavepackets sequences that propagate without overlapping. Second, QSH edge states are helical, meaning that their spin orientation is locked to the group velocity. This means that electron wavepackets propagating in a given direction along the edge are characterized by a well defined spin polarization. For all these reasons, QSH edge states may be a promising platform for electron quantum optics [27–33].

In order to generate electron wave packets in a controlled way, photoexcitation is perhaps the most customary approach. However, QSH edge states exhibit an important difference with respect to customary optoelectronics systems: the vertical electric dipole transitions that typically occur between valence and conduction bands of conventional semiconductors are forbidden in QSH edge states, due to a selection rule arising from their helical nature. To tackle this problem, some works have proposed to exploit circularly polarised radiations, whose magnetic field can induce magnetic dipole transitions on the edge states. This approach, relying on Zeeman coupling [34–36] is, however, limited by the rather small g-factor. Alternatively, it is possible to induce optical transitions from the edge states to the bulk states [35,37] thereby losing, however, the topological protection from disorder, which is one of the most interesting features of topological systems. Most of these approaches are based on what is known in optoelectronics as the *far field* regime, where a monochromatic radiation is applied over the whole sample for a duration that is long compared to its oscillation period.

In this article, we show that in the so called *near field* regime the photoexcitation in QSH edge states is possible without invoking the bulk states or the Zeeman coupling: when the electric field is applied on a spatially *localised* region and for a *finite time*, one can photoexcite localised electron wave packets that propagate with a density profile that maintains its shape unaltered, without dispersion and with a well specified spin polarization. Such photoexcited space density profile is independent of the temperature, of the initial equilibrium state and depends only – and linearly– on the intensity of the applied pulse. These properties, which are derived exactly, are due to the linearity of the spectrum and the chiral anomaly effect characterizing

QSH edge states, and do not rely on any linear response assumption. We also show that the energy correlations induced by the photoexcitation depend on the initial temperature, and that the photoexcited energy distribution does not merely amount to particle-hole excitations, i.e., to a reshuffling of electron states from below to above the equilibrium Fermi level as a result of the electric pulse. Instead, due to the chiral anomaly effect, the electric pulse effectively gives rise to a net creation of charge of one electron branch (compensated by the annihilation of charges of the opposite branch) and under appropriate circumstances one can generate minimal (i.e., purely particle or hole) excitations in each QSH helical branch. So far, these excitations, also known as Levitons [38–46], have been observed in ballistic channels in 2DEGs [47–50]. Furthermore, by analyzing the interplay between the photoexcitation process and the presence of Rashba spin–orbit interaction, we show that the latter can be exploited to tailor the shape of the photoexcited QSH wavepackets.

The article is organised as follows. In Section 2 we present the model, briefly recall the goal of the photoexcitation problem, and present the exact solution of the massless Dirac equation coupled to an electromagnetic pulse. Then, in Section 3, we use such result to determine the general expressions for the photoexcited electron density profile and energy correlations induced by the photoexcitation process, pointing out how to obtain gauge-invariant results. In Section 4 we specify such general results to various types of applied electric pulse, computing the photoexcited electron density profile and the photoexcited energy distribution. Finally, in Section 5 we discuss the interplay between the photoexcitation and presence of Rashba spin–orbit interaction, whereas in Section 6 we propose some possible experimental realization schemes. We finally summarize and conclude in Section 7.

2 Model for photoexcitation in QSH edge states

2.1 Hamiltonian

Let us focus on one edge of a QSH system and denote by x the coordinate along the boundary. A Kramers' pair of one-dimensional (1D) counterflowing helical states is described by a spinor field operator $\Psi(x) = (\psi_\uparrow(x), \psi_\downarrow(x))^T$, where $\uparrow$ and $\downarrow$ refer to the QSH edge spin orientation. The electronic system, initially in an equilibrium state, is then exposed to an externally applied electric field, expressed as

$$E(x,t) = -\partial_x V - \partial_t A/c \tag{1}$$

in terms of scalar and vector potential, V and A, respectively. Here c is the speed of light. The full Hamiltonian thus reads

$$\hat{\mathcal{H}} = \hat{\mathcal{H}}_\circ + \hat{\mathcal{H}}_{em}, \tag{2}$$

where $\hat{\mathcal{H}}_\circ$ denotes the electronic contribution, while

$$\hat{\mathcal{H}}_{em} = e \int dx\, V(x,t)\, \hat{n} - \frac{e}{c} \int dx\, A(x,t)\, \hat{J} \tag{3}$$

describes the coupling to the electromagnetic field, where

$$\hat{n} = \Psi^\dagger(x)\Psi(x) = \hat{n}_\uparrow + \hat{n}_\downarrow \tag{4}$$

is the total electron density operator, with $\hat{n}_\sigma \doteq \psi_\sigma^\dagger \psi_\sigma (\sigma = \uparrow, \downarrow)$ denoting the spin-resolved density, and $\hat{J}$ is the current density operator, whose explicit expression depends on the electronic term $\hat{\mathcal{H}}_\circ$. In particular, we shall mostly focus on the case where the electronic contribution describes the purely linear spectrum of the QSH edge states, and consists of the massless Dirac fermion 'kinetic' term

$$\hat{\mathcal{H}}_\circ = \hat{\mathcal{H}}_{kin} = v_F \int dx \, \Psi^\dagger(x) \, \sigma_3 p_x \, \Psi(x) \tag{5}$$

where v_F is the Fermi velocity, $p_x = -i\hbar\partial_x$, and $\sigma_{1,2,3}$ are Pauli matrices. Then, the expression for the electronic current $\hat{J}$ appearing in (3) reads

$$\hat{J} = v_F \Psi^\dagger(x) \, \sigma_3 \Psi(x) = v_F (\hat{n}_\uparrow - \hat{n}_\downarrow). \tag{6}$$

We anticipate, however, that in Section 5 we shall include in $\hat{\mathcal{H}}_\circ$ also the Rashba spin–orbit coupling along the edge, and in that case the expression of $\hat{J}$ gets modified. Finally, the Zeeman coupling ascribed to the magnetic field arising from time-dependence of $E(x,t)$ can be shown to be negligible [33] and will be omitted henceforth.

2.2 Statement of the problem and the gauge invariance issue

In the initial equilibrium state, i.e., before the term (3) is switched on, the space-time evolution of the electron field operator is dictated by the term (5) and is given by

$$\psi_\sigma^\circ(x,t) = \frac{1}{\sqrt{2\pi\hbar v_F}} \int dE e^{-i\frac{E}{\hbar}(t \mp \frac{x}{v_F})} c_{E,\sigma}^\circ \qquad \sigma = \uparrow, \downarrow = \pm, \tag{7}$$

where the correlation between the energy mode operators $c_{E,\sigma}^\circ$

$$\mathcal{G}_\sigma^\circ(E, \tilde{E}) \doteq \left\langle c_{E+\frac{\tilde{E}}{2},\sigma}^{\circ\,\dagger} c_{E-\frac{\tilde{E}}{2},\sigma}^\circ \right\rangle = \delta(\tilde{E}) \, f^\circ(E) \tag{8}$$

is purely diagonal and characterized by the Fermi equilibrium distribution function $f^\circ(E) = [1 + \exp[(E-\mu)/k_B T]]^{-1}$, with chemical potential μ and temperature T. Here energies are measured with respect to the Dirac level. Furthermore, the space profile of the equilibrium density is uniform

$$n_\sigma^\circ = \langle \psi_\sigma^{\circ\,\dagger}(x,t) \psi_\sigma^\circ(x,t) \rangle = \text{const} = \frac{\mu + E_c}{2\pi\hbar v_F} \tag{9}$$

where E_c denotes the ultraviolet energy cut-off of the band dispersion.

When the electric pulse is applied, the system is driven out of equilibrium by the term equation (3), and the space profile, as well as the energy correlations are modified. The goal of the investigation is to determine the photoexcited density profile and energy correlations, i.e., the *deviations* of these quantities with respect to their equilibrium value,

$$\Delta n_\sigma(x,t) \doteq \langle \psi_\sigma^\dagger(x,t)\psi_\sigma(x,t) \rangle - \langle \psi_\sigma^{\circ\,\dagger}(x,t)\psi_\sigma^\circ(x,t) \rangle \tag{10}$$

$$\Delta\mathcal{G}_\sigma(E, \tilde{E}; x) \doteq \langle c_{E+\frac{\tilde{E}}{2},\sigma}^\dagger(x) c_{E-\frac{\tilde{E}}{2},\sigma}(x) \rangle - \langle c_{E+\frac{\tilde{E}}{2},\sigma}^{\circ\,\dagger} c_{E-\frac{\tilde{E}}{2},\sigma}^\circ \rangle \tag{11}$$

where $\psi_\sigma(x,t)$ is the electron field evolution for the full Hamiltonian (2), and the local (i.e., x-dependent) density mode operators, defined as

$$c_{E,\sigma}(x) \doteq \sqrt{\frac{v_F}{2\pi\hbar}} \int dt \, e^{+i\frac{E}{\hbar}(t \mp \frac{x}{v_F})} \psi_\sigma(x,t), \tag{12}$$

identify the energy weight of the electron field operator at the space point x.

Importantly, we observe that the Hamiltonian (2) depends on the specific gauge (V, A) chosen to describe the electric field (1). However, a physically meaningful observable can only depend on the applied electric field, and not on the gauge choice. Thus, the essential prerequisite for a correct result about photoexcitation is that it must be left *invariant* by any gauge transformation

$$\begin{cases} V & \rightarrow & V' = V - (\hbar/e)\partial_t \chi \\ A & \rightarrow & A' = A + (\hbar c/e)\partial_x \chi \\ \Psi(x,t) & \rightarrow & \Psi'(x,t) = e^{i\chi(x,t)}\Psi(x,t) \end{cases} \tag{13}$$

where χ is any arbitrary function. We emphasize that, since gauge invariance issue is tightly connected to the conservation of electrical charge, this aspect cannot be overlooked. In systems described by a linear spectrum (massless Dirac fermions), such requirement involves some subtlelties that are not present in conventional systems described a parabolic spectrum (Schrödinger fermions), as we shall discuss below.

2.3 Exact solution of the massless Dirac equation coupled to an electric field in 1+1 dimensions

In a given gauge (V, A) of electromagnetic potentials, the equations of motion for the electron field operator are dictated by the Hamiltonian (2) with equations (3) and (5), and read

$$i\hbar\partial_t \Psi = \left(v_F \sigma_3 \left(\hat{p} - \frac{e}{c}A(x,t)\right) + eV(x,t)\sigma_0 \right) \Psi, \tag{14}$$

where σ_0 is the 2×2 identity matrix. Equation (14) is the massless Dirac equation coupled to the electromagnetic potentials in 1+1 dimensions. Since the matrix term on the right-hand side is purely diagonal, the equations for the two components $\psi_\uparrow$ and $\psi_\downarrow$ are decoupled and can be solved exactly [32], obtaining

$$\psi_{\uparrow,\downarrow}(x,t) = \psi_{\uparrow,\downarrow}^\circ(x \mp v_F t) \, e^{\pm i\phi_{\uparrow,\downarrow}(x,t)}, \tag{15}$$

where $\psi_{\uparrow,\downarrow}^\circ(x \mp v_F t)$ denotes the space-time evolution of the electron field component of equation (5), i.e., in absence of the electromagnetic coupling, and represents genuine right-moving electrons with spin-$\uparrow$ and left-moving electrons with spin-$\downarrow$, respectively. In contrast, the phases $\phi_{\uparrow,\downarrow}$ encode the effect of the electromagnetic potentials $V(x,t)$ and $A(x,t)$, and can be given two equivalent expressions

$$\begin{aligned} \phi_\uparrow(x,t) &= \frac{ev_F}{\hbar c} \int_{-\infty}^t (A - \frac{c}{v_F}V)(x - v_F(t - t'), t') \, dt' \\ &= \frac{e}{\hbar c} \int_{-\infty}^x (A - \frac{c}{v_F}V)(x', t - \frac{x - x'}{v_F}) \, dx' \end{aligned} \tag{16}$$

and

$$\phi_\downarrow(x,t) = \frac{ev_F}{\hbar c} \int_{-\infty}^{t} (A + \frac{c}{v_F} V)(x + v_F(t - t'), t') \, dt'$$

$$= \frac{e}{\hbar c} \int_{x}^{\infty} (A + \frac{c}{v_F} V)(x', t + \frac{x - x'}{v_F}) \, dx'. \quad (17)$$

The above expressions have a straightforward physical interpretation. The first (second) line of equation (16), for instance, expresses the phase $\phi_\uparrow(x,t)$ induced by the electromagnetic field on the helical right-moving electron $\psi_\uparrow^\circ(x - v_F t)$ as a convolution over time (space) of the values of the electromagnetic potentials at times earlier than t and at positions located on the left of x, propagating with the electron Fermi velocity v_F according to the dynamics dictated by equation (5). It is worth pointing out that the phases (16) and (17) are gauge *dependent*, as they characterize the exact solution of the gauge-dependent equation of motion (14). In the next section we shall show how to obtain gauge *independent* results.

3 General results for photoexcitation

3.1 Photoexited electron density profiles

Since the whole effect of the electromagnetic coupling amounts to the *phases* (16) and (17) that multiply the result ψ_σ° in absence of electric pulse, one might at first naively think that such phases drop out when computing field bilinear from equation (15), such as densities $\hat{n}_\sigma = \psi_\sigma^\dagger \psi_\sigma$ (with $\sigma = \uparrow, \downarrow$). That would mean that the numbers of right- and left-moving electrons are separately conserved, remaining equal to the value $\hat{n}_\sigma^\circ = \psi_\sigma^{\circ\dagger} \psi_\sigma^\circ$ without electric field. One would thus be tempted to conclude that the electric pulse does not alter the equilibrium density profiles ($\Delta\hat{n}_\sigma \equiv 0$) and, in particular, that the *chiral density* $\hat{n}^a = \Psi^\dagger \sigma_3 \Psi = \hat{n}_\uparrow - \hat{n}_\downarrow$ is conserved. This conservation of the chiral density would also seem to agree with Nöther's theorem, following from the existence of the chiral symmetry

$$\begin{cases} \Psi(x,t) \rightarrow \Psi'(x,t) = e^{i\zeta(x,t)\sigma_3}\Psi(x,t) \\ V \quad \rightarrow \quad V' = V - (\hbar/e)\,\sigma_3\,\partial_t\zeta \\ A \quad \rightarrow \quad A' = A + (\hbar c/e)\,\sigma_3\,\partial_x\zeta \end{cases} \quad (18)$$

of the equation of motion (14). However, such conclusion is wrong. The obvious physical reason is that an applied electric field must modify the electron current (6). The mathematical reason is that, despite the existence of such symmetry and the decoupling of the equation (14), the infinite number of states characterizing the Fermi sea leads to an anomalous breaking of Nöther's conservation law. This nontrivial effect is known as the chiral anomaly. Here we shall only summarize the main technical aspects related to the 1+1 dimensional case of QSH edge states (details can be found in Ref. [32]), before describing its effects on the photoexcitation properties. A physically correct photoexcited density must be *finite* and *gauge independent*. In order to fulfill these two requirements, one computes the photoexcited density as

$$\Delta n_\sigma(x,t) \doteq \lim_{(x',t')\to(x,t)} \left\langle \psi_\sigma^\dagger(x',t')\psi_\sigma(x,t)\, e^{-iW_L(x,t,x',t')} - \psi_\sigma^{\circ\dagger}(x',t')\psi_\sigma^\circ(x,t) \right\rangle_\circ, \quad (19)$$

where $\psi_\sigma(x,t)$ is the electron field operator in the presence of the electromagnetic field, equation (15), while $\psi_\sigma^\circ(x,t)$ is the one in absence of electromagnetic field. The point-splitting procedure, which is equivalent to introducing a cut-off in k-space, enables one to regularize the infinite ground state contribution, which is already present without electromagnetic field and can thus be safely subtracted, thereby obtaining a finite result. However, such result would be gauge-dependent since the point-splitting procedure breaks the gauge invariance. Thus, the Wilson line

$$W_L(x,t,x',t') = \frac{\mathrm{e}}{\hbar c} \int_{(x,t)}^{(x',t')} (cV\,dt'' - A\,dx'')$$

(20)

connecting the two split points (x',t') and (x,t) is introduced in equation (19) to restore the gauge invariance, guaranteeing that the result is independent of the specific gauge (V,A) chosen for the electric field (1). Applying the above procedure, and inserting the exact solution (15) into equation (19), one obtains the following equivalent expressions for the photoexcited density profiles [32]

$$
\begin{aligned}
\Delta n_\uparrow(x,t) &= +\frac{\mathrm{e}}{2\pi\hbar} \int_{-\infty}^t E(x - v_F(t-t'), t')\,dt' \\
&= +\frac{\mathrm{e}}{2\pi\hbar v_F} \int_{-\infty}^x E(x', t - \frac{x-x'}{v_F})\,dx' \\
&= +\frac{1}{2\pi} \left(\partial_x \phi_\uparrow(x,t) - \frac{\mathrm{e}}{\hbar c} A(x,t) \right) \\
&= -\frac{1}{2\pi v_F} \left(\partial_t \phi_\uparrow(x,t) + \frac{\mathrm{e}}{\hbar} V(x,t) \right),
\end{aligned}
$$

(21)

and

$$
\begin{aligned}
\Delta n_\downarrow(x,t) &= -\frac{\mathrm{e}}{2\pi\hbar} \int_{-\infty}^t E(x + v_F(t-t'), t')\,dt' \\
&= -\frac{\mathrm{e}}{2\pi\hbar v_F} \int_x^\infty E(x', t + \frac{x-x'}{v_F})\,dx' \\
&= +\frac{1}{2\pi} \left(\partial_x \phi_\downarrow(x,t) + \frac{\mathrm{e}}{\hbar c} A(x,t) \right) \\
&= +\frac{1}{2\pi v_F} \left(\partial_t \phi_\downarrow(x,t) - \frac{\mathrm{e}}{\hbar} V(x,t) \right).
\end{aligned}
$$

(22)

Three comments are in order about this result. First, their gauge invariance clearly appears from the first two lines of equations (21) and (22), which depend only on the electric field. Second, they are exact (as far as the model for linear spectrum holds) and do not rely on any linear response approximation. Third, the profile are independent of the temperature T and of the chemical potential μ of the initial equilibrium state.

3.1.1 Chiral anomaly

By taking time and space derivatives of the first lines of the obtained photoexcited densities equations (21) and (22), one can straightforwardly prove that

$$(\partial_t + v_F \partial_x)\Delta\hat{n}_\uparrow(x,t) = +\frac{\mathrm{e}}{2\pi\hbar}E(x,t)$$
$$(\partial_t - v_F \partial_x)\Delta\hat{n}_\downarrow(x,t) = -\frac{\mathrm{e}}{2\pi\hbar}E(x,t), \tag{23}$$

showing that the electric field $E(x,t)$ breaks the conservation laws appearing on the left hand side, thereby effectively creating and destroying electrons in each branch. Importantly, by taking sum and difference of equation (23) one finds

$$\partial_t \Delta\hat{n}(x,t) + \partial_x \Delta\hat{j}(x,t) = 0 \tag{24}$$
$$\partial_t \Delta\hat{n}^a(x,t) + \partial_x \Delta\hat{j}^a(x,t) = \frac{\mathrm{e}}{\pi\hbar}E(x,t). \tag{25}$$

The continuity equation (24) for the electron charge $\Delta\hat{n} = \Delta\hat{n}_\uparrow + \Delta\hat{n}_\downarrow$ is fulfilled, due to the gauge invariance under equation (13). However, the conservation law involving the axial charge $\Delta\hat{n}^a = \Delta\hat{n}_\uparrow - \Delta\hat{n}_\downarrow$ and axial current $\Delta\hat{j}^a = v_F(\Delta\hat{n}_\uparrow + \Delta\hat{n}_\uparrow)$, which would be expected from the chiral symmetry equation (18), is broken by the anomalous term appearing in equation (25). This is the chiral anomaly effect, first discovered in high energy physics [51–54] and nowadays on the spotlight in condensed matter physics [55–58] both in 3D Weyl semimetals [59–62] and in 1D QSH edge states [63]. Notably, the anomalous term on the r.h.s. of equation (25) [or equivalently in Eq. (23)] depends *only* on the universal constant $\mathrm{e}/2\pi\hbar$ and the electric field $E(x,t)$, and not on the electron degrees of freedom. This shows the close relation between the chiral anomaly and the above mentioned T- and μ-independence of $\Delta n_\sigma(x,t)$ for massless Dirac fermions. Indeed for massive fermions with a non-linear dispersion relation, equation (25) would display an additional (non-anomalous) term, proportional to the mass and dependent on the electronic state [54].

3.2 Photoexcited local energy correlations

Let us now consider the electronic correlations. While in reference [32] we have focussed mostly on the photoexcited momentum distribution, which is a correlation of electron operators at different space points and at the same time $t' = t$, here we shall focus on the local correlation (i.e., at equal space point $x' = x$) at different times, described by

$$\mathcal{G}_\sigma(t_2,t_1;x) \doteq e^{-\frac{i e}{\hbar}\int_{t_2}^{t_1} V(x',t)\,dt'} \left\langle \psi_\sigma^\dagger(x,t_1)\psi_\sigma(x,t_2)\right\rangle \qquad \sigma = \uparrow,\downarrow, \tag{26}$$

where the phase pre-factor involving the scalar potential V is nothing but the Wilson line (20) in the particular case of equal space point correlations $x' = x$, and guarantees the gauge invariance of the equation (26). By Fourier transforming equation (26) with respect to the time difference $t' = t_1 - t_2$ and the average time $t = (t_1 + t_2)/2$, one obtains the correlation in the energy domain,

$$\mathcal{G}_\sigma(E,\tilde{E};x) = \frac{v_F}{2\pi\hbar}\iint dt\,dt'\, e^{-i\frac{Et'}{\hbar}}e^{-i\frac{\tilde{E}t}{\hbar}}\mathcal{G}_\sigma(t-\frac{t'}{2},t+\frac{t'}{2};x). \tag{27}$$

Inserting the exact space-time evolution obtained in equation (15) for the electron field operator into equations (26) and (27), one expresses the energy correlation as

$$\mathcal{G}_{\uparrow,\downarrow}(E,\tilde{E};x) = \frac{1}{4\pi\hbar}\int_{-\infty}^{+\infty}dt\, e^{-i\tilde{E}t/\hbar}\left(-i\lim_{a\to 0}\int_{-\infty}^{+\infty}\frac{e^{\mp i\Delta\phi_{\uparrow,\downarrow}^{\mathrm{es}}(t,t';x)}e^{-i(E-\mu)t'/\hbar}}{l_T\sinh[\pi(v_F t'-ia)/l_T]}\,d(v_F t')\right),$$

(28)

where $l_T = \hbar v_F/k_B T$ is the thermal lengthscale related to the equilibrium temperature T, whereas $a = \hbar v_F/E_c$ is a short distance related to the ultra-violet energy cutoff E_c. Furthermore, the dimensionless quantity

$$\Delta\phi_{\uparrow,\downarrow}^{\mathrm{es}}(t,t';x) \doteq \phi_{\uparrow,\downarrow}(x,t+\frac{t'}{2}) - \phi_{\uparrow,\downarrow}(x,t-\frac{t'}{2}) \pm \frac{\mathrm{e}}{\hbar}\int_{t-\frac{t'}{2}}^{t+\frac{t'}{2}}V(x,t')\,dt' \quad (29)$$

denotes the *gauge invariant* phase difference at equal space (es) points $x = x'$, where the second term on the right-hand side compensates for the gauge dependence of the first term $\phi_{\uparrow,\downarrow}$, given by equations (16) and (17).

In particular, for the initial equilibrium state the correlation (26) is given by

$$\mathcal{G}_{\sigma}^{\circ}(t_2,t_1;x) = \langle\psi_{\sigma}^{\circ\dagger}(x,t_1)\psi_{\sigma}^{\circ}(x,t_2)\rangle_{\circ} = -i\,\frac{e^{i\mu(t_1-t_2)/\hbar}}{2l_T\sinh\left[\pi v_F(t_1-t_2-\frac{i\hbar}{E_c})/l_T\right]}, \quad (30)$$

and depends only on the time difference. Thus, once inserted into equation (27), it straightforwardly yields the diagonal equilibrium energy correlation (8), which vanishes for any $\tilde{E}\neq 0$.

In contrast, when the time-dependent electric pulse is applied, the out of equilibrium correlation (26) does not necessarily depend on the difference $t' = t_1 - t_2$ between the two time arguments, due to the phase difference (29) and the Wilson prefactor. Thus, the photoexcited energy distribution, i.e., the deviation of equation (28) from the equilibrium value (8), also contain 'off-diagonal' terms $\tilde{E}\neq 0$, and can be expressed as

$$\Delta\mathcal{G}_{\uparrow,\downarrow}(E,\tilde{E};x) = \mp\frac{1}{4\pi\hbar}\frac{1}{l_T}\int_{-\infty}^{+\infty}dt\, e^{-i\tilde{E}t/\hbar}$$

$$\times\int_{-\infty}^{+\infty}\frac{\sin\left[\Delta\phi_{\uparrow,\downarrow}^{\mathrm{es}}(t,t';x)\pm(E-\mu)t'/\hbar\right]\mp\sin\left[(E-\mu)t'/\hbar\right]}{\sinh[\pi v_F t'/l_T]}\,d(v_F t').$$

(31)

The photoexcited energy distribution is obtained as the diagonal term $\tilde{E}\to 0$ of the photoexcited energy correlations, i.e.,

$$\Delta\nu_{\uparrow,\downarrow}(E;x) \doteq \Delta\mathcal{G}_{\uparrow,\downarrow}(E,\tilde{E}=0;x). \quad (32)$$

4 Explicit results for specific cases

4.1 Plane wave pulse

In order to appreciate the role of the finite duration of the applied electric pulse, let us first consider the case where a plane wave is applied for a time duration τ

$$E(x,t) = E_0 \, \theta(\frac{\tau}{2} - t)\theta(\frac{\tau}{2} + t) \, \cos(\frac{\Omega x}{c}) \, \cos(\Omega t), \qquad (33)$$

where Ω and τ are the frequency the duration of the pulse, respectively, and θ denotes the Heaviside function. Applying the general result equations (21) and (22) to equation (33), and focussing on the times $t > \tau/2$ after the end of the pulse, one finds

$$\Delta n_{\uparrow,\downarrow}(x,t) = \pm \frac{eE_0}{2\pi\hbar\Omega} \left(\sum_{r=\pm} \frac{\sin\left[\Omega\tau(1 + r\frac{v_F}{c})/2\right]}{(1 + r\frac{v_F}{c})} \right) \cos\left[\frac{\Omega}{c}(x \mp v_F t)\right] \qquad t > \frac{\tau}{2} \; .$$
$$(34)$$

We can now consider two limits of equation (34). For a long pulse and/or high frequency ($\Omega\tau \gg 1$) one straightforwardly sees that the photoexcited density profiles vanishes,

$$\Delta n_{\uparrow,\downarrow}(x,t) = \pm \frac{eE_0}{2\hbar\Omega} \cos\left[\frac{\Omega}{c}(x \mp v_F t)\right] \left(\delta(1 + \frac{v_F}{c}) + \delta(1 - \frac{v_F}{c})\right) = 0. \qquad (35)$$

In this case the electron system probes the whole plane wave both in space and time, and momentum and energy conservation laws lead to a vanishing response: there cannot be intra-branch transitions because of the difference between the electron Fermi velocity v_F and the speed of light c.

In contrast, in the case of a short pulse and/or low frequency ($\Omega\tau \ll 1$) one finds

$$\Delta n_{\uparrow,\downarrow}(x,t) = \pm \frac{eE_0\tau}{2\pi\hbar} \cos\left[\frac{\Omega}{c}(x \mp v_F t)\right]. \qquad (36)$$

In this situation only the momentum $q = \Omega/c$ is conserved, whereas energy is not, so that the electron density propagates oscillating in time with a frequency

$$\Omega_{el} = \Omega v_F/c \qquad (37)$$

lower than the frequency Ω of the electromagnetic wave. In particular, denoting by L the size of the system, in the customary situation $\Omega L/c \ll 1$, one obtains

$$\Delta n_{\uparrow,\downarrow}(x,t) \simeq \pm \frac{eE_0\tau}{2\pi\hbar} \cos\left[\frac{v_F}{c}\Omega t\right] \qquad (38)$$

i.e., the electron system sees a spatially uniform field that oscillates in time with a lower frequency $\Omega_{el} = \Omega v_F/c$, and the charge distribution is also uniform.

4.2 Gaussian electric pulse

Let us now consider the case of an electric field that is localized both in time and space. In particular, a Gaussian electric pulse is described by

$$E(x,t) = E_0\, e^{-\frac{x^2}{2\Delta^2}}\, e^{-\frac{t^2}{2\tau^2}}, \tag{39}$$

where Δ and τ denote its space extension and time duration around the space and time origin, respectively, and E_0 is its amplitude. Here below we present the result for the case (39), focussing on the density space profile and the energy distribution of the photoexcited wave packets. Substituting the pulse (39) into equations (21) and (22), one obtains

$$\Delta n_{\uparrow,\downarrow}(x,t) = \pm\frac{eE_0}{2\pi\hbar}\frac{D}{v_F}\sqrt{\frac{\pi}{2}}e^{-\frac{(x\mp v_F t)^2}{2(\Delta^2+(v_F\tau)^2)}}\left[1+\mathrm{Erf}\left(\frac{D}{\sqrt{2}}\left(\pm\frac{x}{\Delta^2}+\frac{t}{v_F\tau^2}\right)\right)\right]$$

where

$$D \doteq \frac{v_F\tau\Delta}{\sqrt{\Delta^2+(v_F\tau)^2}} \tag{40}$$

is an effective length scale involving both the space extension Δ and the time duration τ of the pulse. At long times ($t \gg \tau$) and away from the region of applied pulse ($\sigma x \gg \Delta$), the argument of Error function is large, and one can find the asymptotic expression

$$\Delta n_{\uparrow,\downarrow}(x,t) \simeq \pm\frac{eE_0}{2\pi\hbar}\frac{\tau\Delta\sqrt{2\pi}}{\sqrt{\Delta^2+(v_F\tau)^2}}e^{-\frac{(x\mp v_F t)^2}{2(\Delta^2+(v_F\tau)^2)}}, \tag{41}$$

which describes two spin-polarised photoexcited wave packets propagating rightwards and leftwards, respectively. Notice that the shape of the electron densities $\Delta n_{\uparrow,\downarrow}$ is Gaussian. However, the space extention

$$\Delta_{el} = \sqrt{\Delta^2+(v_F\tau)^2} \tag{42}$$

depends on *both* the space extension Δ and the time duration τ of the electric pulse, and is bigger than Δ.

4.3 Spatial δ-pulses

In the particular limit where the electric pulse is applied over a short region, $\Delta \ll v_F\tau$, equation (39) can be treated as a spatial δ-pulse, $E(x,t) = \mathcal{E}_0\,\delta(x)\exp(-t^2/2\tau^2)$ upon identifying $\mathcal{E}_0 = E_0\Delta\sqrt{2\pi}$. In this case the spatial extension (42) of the photoexcited electron density profile is only given by $\Delta_{el} \simeq v_F\tau$, where τ is the pulse duration. This is a particular case of a spatial δ-pulse. Let us thus analyze this situation in more general terms, allowing for a generic time dependence $\mathcal{V}(t)$ for the spatial δ-pulse centered around $x = 0$,

$$E(x,t) = \delta(x)\,\mathcal{V}(t) \tag{43}$$

where $[\mathcal{V}]$ = voltage. Among all possible gauges reproducing the electric pulse equation (43), two are worth being mentioned,

$$\text{(pure } A\text{-gauge)} \qquad \begin{cases} V & = 0 \\ A(x,t) = -c\,\delta(x) \int_{-\infty}^{t} \mathcal{V}(t')\,dt' \end{cases} \tag{44}$$

$$\text{(pure } V\text{-gauge)} \qquad \begin{cases} V(x,t) = \theta(-x)\,\mathcal{V}(t) \\ A & = 0. \end{cases} \tag{45}$$

The photoexcited density profiles are obtained by inserting equation (43) into the general result (21) and (22), obtaining

$$\Delta n_{\uparrow,\downarrow}(x,t) = \pm \frac{e}{2\pi\hbar v_F} \theta(\pm x)\mathcal{V}\left(t \mp \frac{x}{v_F}\right), \tag{46}$$

whence we see that the *spatial shape* of two counter-propagating spin polarized wavepackets is determined by the *time profile* $\mathcal{V}$ of the pulse.

The phases induced by the electromagnetic field are obtained from the general results (16) and (17) and, in particular for the two gauges (45) and (44), one gets

$$\text{(pure } A\text{-gauge)} \quad \phi_{\uparrow,\downarrow}(x,t) = -\frac{e}{\hbar}\theta(\pm x) \int_{-\infty}^{t \mp \frac{x}{v_F}} \mathcal{V}(t'')\,dt'' \tag{47}$$

$$\text{(pure } V\text{-gauge)} \quad \phi_{\uparrow,\downarrow}(x,t) = -\frac{e}{\hbar}\theta(\pm x) \int_{-\infty}^{t \mp \frac{x}{v_F}} \mathcal{V}(t')\,dt' \mp \frac{e}{\hbar}\theta(-x) \int_{-\infty}^{t} \mathcal{V}(t')\,dt' \tag{48}$$

while the gauge invariant phase difference equation (29) determining the photoinduced energy correlations through equation (31) is given by

$$\Delta\phi_{\uparrow,\downarrow}^{\text{es}}(t,t';x) = -\frac{e}{\hbar}\theta(\pm x) \int_{t \mp \frac{x}{v_F} - \frac{t'}{2}}^{t \mp \frac{x}{v_F} + \frac{t'}{2}} \mathcal{V}(t'')\,dt''. \tag{49}$$

4.3.1 The case of a localized Lorentzian pulse

Let us consider as a specific example the case of spatial δ-pulse (43) with a Lorentzian time shape,

$$\mathcal{V}(t) = \frac{2\hbar u_0}{e} \frac{\tau}{t^2 + \tau^2} \tag{50}$$

where u_0 is a dimensionless amplitude parameter and τ is the duration timescale.

The photoexcited density profiles are straightforwardly obtained from equation (46)

$$\Delta n_{\uparrow,\downarrow}(x,t) = \pm \theta(\pm x) \frac{u_0}{\pi v_F \tau} \frac{(v_F \tau)^2}{(x \mp v_F \tau)^2 + (v_F \tau)^2} \tag{51}$$

and are depicted in Figure 1, where the different curves refer to various time snapshots. We emphasize that, from the general result of reference [32] presented in Section 3.1, the density profile (51) is temperature independent for arbitrary u_0. This was also confirmed for the case $u_0 = 1$ in reference [44].
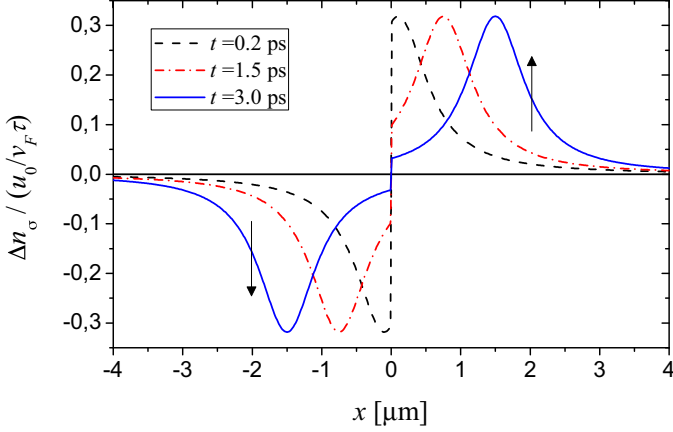
Fig. 1. Photoexcited electron density profiles, generated by a spatial δ-pulse with Lorentzian time profile characterized by $\tau = 1\,\mathrm{ps}$ [see Eqs. (43) and (50)], and are plotted as a function of the distance along the QSH edge from the location of the pulse $x = 0$, at different time snapshots, $t = 0.2\,\mathrm{ps}$ (black dashed curve), $t = 1.5\,\mathrm{ps}$ (red dash-dotted curve) and $t = 3\,\mathrm{ps}$ (blue solid curve). The two wavepackets propagate in opposite directions with opposite spin. Their space profile maintains unaltered without dispersion and is independent of the temperature of initial equilibrium state, due to the linearity of QSH helical edge states spectrum. The value $v_F = 5 \times 10^5\,\mathrm{m/s}$ is taken for the QSH edge Fermi velocity.

As one can see, two spin-polarised wavepackets are gradually generated at the origin $x = 0$, where the pulse is applied, and start to travel in opposite directions with a Lorentzian spatial shape with a spatial extension $v_F\tau$. We emphasize that (i) the photoexcited density profile preserves its shape without any dispersion and (ii) is independent of the temperature and the chemical potential of the initial equilibrium state [32]. Both these features are due to the linearity of the massless Dirac spectrum of QSH edge states. Indeed similar features have been recently found in metallic carbon nanotubes [64] also described by a similar model.

Let us now consider the energy correlations induced by the photoexcitation. To this purpose, we first derive from equation (49) the gauge invariant phase difference, obtaining

$$\Delta\phi^{\mathrm{es}}_{\uparrow,\downarrow}(t,t';x) = -2u_0\theta(\pm x)\left(\arctan\left(\frac{t+\frac{t'}{2}}{\tau}\right) - \arctan\left(\frac{t-\frac{t'}{2}}{\tau}\right)\right) \qquad (52)$$

and then insert it in equation (31). From equation (52) we note that $\Delta\phi^{\mathrm{es}}_{\uparrow}(t,t';x) = \Delta\phi^{\mathrm{es}}_{\downarrow}(t,t';-x)$ and we can then deduce from equation (31) the general relation

$$\Delta\mathcal{G}_{\downarrow}(E-\mu,\tilde{E};x) = -\Delta\mathcal{G}_{\uparrow}(\mu-E,\tilde{E};-x). \qquad (53)$$

It is therefore enough to compute only $\Delta\mathcal{G}_{\uparrow}$. In particular, we shall focus on the diagonal limit $\tilde{E} \to 0$ [see Eq. (32)], which describes the photoexcited energy distribution, i.e., the deviation from the equilibrium Fermi distribution (8). The result is plotted in Figure 2 as a function of energy deviation from the equilibrium Fermi level, for two values of the Lorentzian amplitude parameter, $u_0 = 0.7$ in panel (a) and $u_0 = 1$ in panel (b). Two important aspects emerge. The first one can be deduced by inspecting the various curves, which describe the behavior of $\Delta\nu_{\uparrow}(E;x)$ for different values of temperatures. The photoexcited energy distribution $\Delta\nu_{\uparrow}(E;x)$ does depend on the
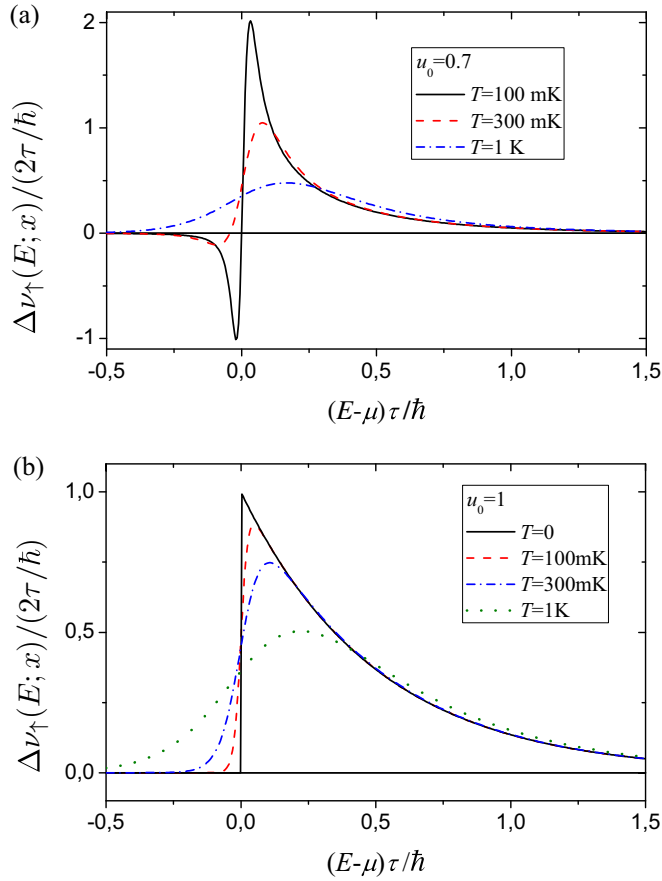
Fig. 2. The energy distribution equation (32) of the spin-↑ electrons photoexcited by a space δ-pulse is plotted as a function of the energy deviation from the initial equilibrium chemical potential μ, in units of $2\tau/\hbar$. The time shape of the pulse is Lorentzian, equation (50), with time parameter $\tau = 1\,\mathrm{ps}$ and amplitude parameter $u_0 = 0.7$ [panel (a)], and $u_0 = 1$ [panel (b)]. The various curves refer to different temperatures, whose values are indicated in the legenda, and are essentially independent of the location x, due to the fact that the pulse is applied over a very narrow δ-like region. In both cases it appears that $\Delta\nu_\uparrow(E;x)$ depends on temperature, quite differently from the spatial density profile (see Fig. 1) and that the integral of $\Delta\nu_\uparrow(E;x)$ over energy is not vanishing: the photoexcitation process does not simply redistribute electrons from below to above the Fermi level, a clear signature of the chiral anomaly effect characterizing QSH edge states. In particular, the case (b) describes purely particle excitations, also known as Levitons, whose zero temperature expression is given by equation (55).

temperature T and on the chemical potential μ of the initial equilibrium state. On the one hand, this can easily be understood from the fact that the equilibrium distribution characterizing the initial state occupancy determines which states are available for the photoexcitation process. On the other hand, this is quite different from the photoexcited density profiles $\Delta n_{\uparrow,\downarrow}(x,t)$ [see Eqs. (21) and (22)], which are temperature independent. This means that, for QSH edge states, despite the redistribution induced by the photoexcitation process on the energy depends on the initial state, it always occurs in such a way that the corresponding density profile is insensitive to such initial state. For the sake of clarity, it is worth recalling that the photoexcited

energy distribution is not the Fourier transform of the photoexcited density space profile (which a local quantity in space and time), as the former takes into account also the correlations at *different* times at that space point. This is why the essential difference in terms of the temperature behavior emerges.

The second noteworthy aspect emerging from Figure 2a is that, although the curves in general display a depletion (hole excitations) below the Fermi energy and and enhancement (particle excitations) above the Fermi level, the integral of $\Delta\nu_\uparrow(E;x)$ over energy is typically not zero. This means that, in general, the photoexcitation process in QSH edge states does not simply generate particle-hole excitations by reshuffling states from below to above the Fermi level and viceversa. Indeed, besides this particle-hole contribution, there exists a net charge 'creation' effect for spin-$\uparrow$ electrons. This appears clearly in the case $u_0 = 1$, shown in Figure 2b, where the photoexcitation generates purely particle excitations above the Fermi level, without holes. Such effective creation effect is a result of the infinite number of states characterizing the ground state of Dirac fermions: the applied electric pulse pulls up states from the depth of the Fermi sea so that, in comparison with the equilibrium state, a net charge is generated. This 'creation' is of course compensated by the annihilation effect of spin-$\downarrow$ electrons, $\Delta\nu_\downarrow^\circ(E-\mu;x) = -\Delta\nu_\uparrow^\circ(\mu-E;-x)$, as can be deduced by equation (53), consistently with the fact that no net charge can be created by an electromagnetic pulse (the careful treatment of gauge invariance precisely guarantees that the total charge of the system is conserved). This is the gist of the chiral anomaly effect characterizing massless Dirac fermions [53]. Although the two spin components are not coupled directly by the electromagnetic field, they are coupled indirectly via the infinite depth of the Fermi sea. This physically means that, above the QSH bulk gap, the edge channels get coupled through the bulk states of the QSH quantum well. A similar situation occurs in one-dimensional ballistic channels of a 2DEG, where only near the Fermi level can the parabolic spectrum be well approximated by two decoupled linear branches of right- and left-moving electrons. However, near the band bottom such decoupling is not well defined and the hole left at the bottom of the Fermi sea by a (say) photoexcited right-moving electron can be occupied by a left-moving electron, which in turn leaves a hole at the other Fermi point [40].

The peculiarity of the case $u_0 = 1$ shown in Figure 2b was first noticed by Levitov and coworkers [38–40], and can be rigorously proven by noticing that, in such case, the exponential factor $e^{-i\Delta\phi_\uparrow(t,t';x)}$ appearing in equation (28) reduces to

$$e^{-i\Delta\phi_\uparrow(t,t';x)}\Big|_{u_0=1} = \prod_{r=\pm} \frac{t' + 2rt - 2i\tau}{t' + 2rt + 2i\tau}, \qquad (54)$$

which is an analytical function in the upper half-plane of t'. Thus, when $E < \mu$, a closing of the integral contour of equation (28) in such half-plane only leaves the equilibrium contribution. A non vanishing photoexcited local energy distribution can only be found above the equilibrium Fermi level (purely particle excitation). Explicitly, at zero temperature and $u_0 = 1$ one finds

$$\Delta\nu_\uparrow(E;x)|_{T=0\,;\,u_0=1} = \theta(x)\,\theta(E-\mu)\,\frac{2\tau}{\hbar}\,e^{-2|E-\mu|\tau/\hbar} \qquad (55)$$

and, more in general, for the photoexcited energy correlations

$$\Delta\mathcal{G}_{\uparrow,\downarrow}(E,\tilde{E};x)\Big|_{T=0\,;\,u_0=1} = \pm\theta(\pm x)\,\theta(\pm(E-\mu))\,e^{\mp i\tilde{E}x/\hbar v_F}\,\frac{2\tau}{\hbar}\cdot e^{-2|E-\mu|\tau/\hbar}$$
$$\times \Big(\mathrm{sgn}[2|E-\mu|+\tilde{E}] + \mathrm{sgn}[2|E-\mu|-\tilde{E}]\Big)/2 \qquad (56)$$

Note that equation (56) is independent of the position x. The existence of such minimal excitations, also called Levitons, is currently on the spotlight in electron quantum optics [41–46], especially after their experimental observation in ballistic channels of a 2DEG [47–50] and the proposal of their detection in QH systems [65].

5 Interplay between photoexcitation and Rashba spin–orbit coupling

In QSH systems, besides the bulk spin–orbit coupling underlying the topological transition and giving rise to the very existence of the edge states, Rashba spin–orbit coupling (RSOC) can emerge along the edge either because of disorder effects, due to the random ion distribution in the heterostructure doping layers and to the random bonds at the quantum well interfaces [66,67], or by intentional deformation of the boundary curvature [68–72] or also by the electric field itself applied to local metallic gate electrodes, e.g., to generate the electric pulse for the photoexcitation [73–76]. For these reasons, we wish to address the interplay between RSOC and photoexcitation. In the presence of RSOC, the electronic term appearing in (2) becomes

$$\hat{\mathcal{H}}_\circ = \hat{\mathcal{H}}_{kin} + \hat{\mathcal{H}}_R \tag{57}$$

where the Rashba-coupling term

$$\hat{\mathcal{H}}_R = \frac{1}{\hbar} \int dx\, \Psi^\dagger(x)\, \frac{1}{2} \left\{ \alpha_R(x), p_x \right\} \sigma_2\, \Psi(x) \tag{58}$$

is characterised by a profile $\alpha_R(x)$ and depends linearly on the momentum p_x. As a consequence, the current operator $\hat{J}$ appearing in the electromagnetic coupling (3) is modified into

$$\hat{J} = v_F \Psi^\dagger(x) \left(\sigma_3 + \frac{\alpha_R(x)}{\hbar v_F} \sigma_2 \right) \Psi(x) = v_F \left[\hat{n}_\uparrow - \hat{n}_\downarrow + \frac{i\alpha_R(x)}{\hbar v_F} (\psi_\downarrow^\dagger \psi_\uparrow - \psi_\uparrow^\dagger \psi_\downarrow) \right] \tag{59}$$

in order to ensure charge conservation. The Hamiltonian (2) can be compactly rewritten as $\hat{\mathcal{H}} = \int dx\, \Psi^\dagger(x)\, H(x)\, \Psi(x)$, where the first-quantized Hamiltonian density is

$$H(x) = \frac{v_F}{2} \left\{ \sigma_3 + \tan\theta_R(x)\sigma_2\,, p_x - \frac{e}{c} A(x,t) \right\} + eV(x,t)\sigma_0, \tag{60}$$

with σ_0 denoting the 2×2 identity matrix and $\theta_R \in [-\pi/2; +\pi/2]$ is the Rashba angle, defined as

$$\theta_R(x) \doteq \arctan \frac{\alpha_R(x)}{\hbar v_F}. \tag{61}$$

Due to the RSOC, the Hamiltonian (60) is no longer diagonal, and the dynamics of the spin components $\psi_\uparrow$ and $\psi_\downarrow$ is coupled. This suggests that the field Ψ, i.e., the basis of spin components, is not the most suitable one to obtain the dynamical evolution. Instead, it is worth switching to another basis, by re-expressing the electron field spinor Ψ as a rotation around σ_1 by the space-dependent Rashba angle $\theta_R(x)$

$$\Psi(x) \doteq e^{+\frac{i}{2}\sigma_1\theta_R(x)}\, \mathrm{X}(x) \tag{62}$$

where

$$X(x) = \begin{pmatrix} \chi_+(x) \\ \chi_-(x) \end{pmatrix} \tag{63}$$

is called the "chiral" field spinor. The rotation (62) enables one to rewrite the Hamiltonian (2) as $\hat{\mathcal{H}} = \int dx\, \Psi^\dagger(x) H(x) \Psi(x) = \int dx\, X^\dagger(x) H_\chi(x) X(x)$, where

$$H_\chi(x) = \frac{1}{2} \left\{ v(x), p_x - \frac{e}{c} A(x,t) \right\} \sigma_3 + eV(x,t)\sigma_0 \tag{64}$$

is the Hamiltonian of massless Dirac fermions travelling with a *space-dependent* velocity profile

$$v(x) = \frac{v_F}{\cos\theta_R(x)} = v_F \sqrt{1 + \left(\frac{\alpha_R(x)}{\hbar v_F} \right)^2} \geq v_F \tag{65}$$

and exposed to the electromagnetic field. In the chiral basis (63) the RSOC, encoded in the profile (65), always *increases* the velocity with respect to the bare value of Fermi velocity v_F, regardless of the sign of α_R. Furthermore, in the chiral basis the density (4) and the current density (6) acquire simple expressions, namely $\hat{n}(x) = X^\dagger(x) X(x) = \hat{n}_+ + \hat{n}_-$ and $\hat{J}(x) = v(x) X^\dagger(x)\sigma_3 X(x) = v(x)(\hat{n}_+ - \hat{n}_-)$, with $\hat{n}_\pm \doteq \chi_\pm^\dagger \chi_\pm$. Finally we emphasise that, since H_χ is diagonal in the chiral basis [see Eq. (64)], the two components $\chi_\pm$ of equation (63) are dynamically *decoupled*, even when the electromagnetic field is applied and the RSOC is present. This feature implies that, in striking contrast with the original spin components $\psi_\uparrow$ and $\psi_\downarrow$, which have a well defined propagation direction only away from the Rashba interaction region, the chiral components χ_+ and χ_- describe genuine right-moving and left-moving electrons, respectively, even in the regions where Rashba interaction is present. This is the origin of the term "chiral" and the reason for considering X as the "natural basis" for Rashba-coupled states.

In the chiral basis it is now easy to generalize the results obtained in Section 2 to the case of an inhomogeneous velocity. The dynamical evolution of the electron field operator is given by

$$\left(\partial_t \pm v(x)\partial_x \pm \frac{1}{2}\partial_x v(x) \right) \chi_\pm = -\frac{ie}{\hbar} \left(V(x,t) \mp \frac{v(x)}{c} A(x,t) \right) \chi_\pm, \tag{66}$$

whose solution is [33]

$$\chi_\pm(x,t) = e^{\pm i\phi_\pm(x,t)} \chi_\pm^\circ(x,t). \tag{67}$$

Here

$$\chi_\pm^\circ(x,t) = \frac{1}{\sqrt{2\pi\hbar\, v(x)}} \int dE\, e^{-i\frac{E}{\hbar}\left(t \mp \int_{x_r}^x \frac{dx''}{v(x'')} \right)} \hat{c}_{E\pm} \tag{68}$$

is a solution for the pulse-free case, equation (57), where the exponential phases clearly show that $\chi_\pm^\circ$ are genuine right- and left-moving electrons, respectively, propagating with the inhomogeneous velocity (65), while $\hat{c}_{E+}$ and $\hat{c}_{E-}$ denote fermionic operators for right- and left-moving electrons at the energy E, fulfilling $\{\hat{c}_{E\pm}, \hat{c}_{E'\pm}^\dagger\}$

$= \delta(E - E')$, and x_r denotes an arbitrarily fixed reference point, such as the space origin or the geometrical center of the RSOC profile. Furthermore, in equation (67)

$$\phi_+(x,t) = \frac{e}{\hbar c} \int_{-\infty}^x dx' \left(A - \frac{c}{v(x')} V \right) \left(x', t - \int_{x'}^x \frac{dx''}{v(x'')} \right)$$

$$\phi_-(x,t) = \frac{e}{\hbar c} \int_x^\infty dx' \left(A + \frac{c}{v(x')} V \right) \left(x', t - \int_x^{x'} \frac{dx''}{v(x'')} \right)$$

(69)

describe the phases induced by the electromagnetic field, and generalize the expressions (16) and (17) obtained without RSOC. The result (67) thus describes *exactly* – within the assumption of independent electrons – the electron dynamics in the presence of both the RSOC and the electromagnetic field.

Proceeding in a similar way as was done in Section 3, one obtains the expressions for the right- and left-moving photoexcited density profiles $\Delta n_\pm$, namely

$$\Delta n_+(x,t) = +\frac{e}{2\pi\hbar v(x)} \int_{-\infty}^x dx' E(x', t - \int_{x'}^x \frac{dx''}{v(x'')})$$

(70)

$$\Delta n_-(x,t) = -\frac{e}{2\pi\hbar v(x)} \int_x^\infty dx' E(x', t - \int_x^{x'} \frac{dx''}{v(x'')}),$$

(71)

which are shown in Figure 3, where the interplay of a Gaussian electric pulse (39) with a RSOC region (grey area) is described. Because of the inhomogeneous Fermi velocity (65) induced by the RSOC, the electrons photoexcited inside and outside the RSOC region have different Fermi velocities, generating the fuzzy shape of the wavepackets. This interplay shows that the RSOC can be exploited to tailor the shape of photoexcited wavepackets. Other examples and a thorough discussion of these effects can be found in reference [33].

6 Proposal for experimental realisations

Two main realisations of QSH systems presently exist, namely in HgTe/CdTe [18–22] and in InAs/GaSb [23–26] quantum wells. In their topological phase, conducting helical edge states appear and exhibit a linear dispersion with a Fermi velocity $v_F \simeq 5 \times 10^5$ m/s and $v_F \simeq 2 \times 10^4$ m/s, respectively [20,25], within a bulk gap $E_g \sim 30$ meV. The phase breaking length L_ϕ, i.e., the length scale for which the analysis carried out in this paper is valid, is of the order of a few micrometers at Kelvin temperatures.

A localised electromagnetic pulse can be generated with two techniques. The first one is the use of near field scanning optical microscopy operating in the illumination mode: an optical fiber with a thin aperture of tens of nanometers, positioned near the edge, excites a strong electric field at the tip apex [77–81]. With this sophisticated technique one obtains localised pulses, whose spatial center can also be easily displaced. The second approach to create a localised electromagnetic pulse is somewhat more straightforward: it consists in utilising side finger gate electrodes, deposited close to a boundary of the QSH bar and biased by time-dependent voltages experienced by the electrons in the edge [82], similarly to what has been proposed for a 2DEG [11,40,47–50]. In this case the spatial extension of the electric pulse is determined by the lateral width of the finger electrode, $\sim$100 nm, which can be biased
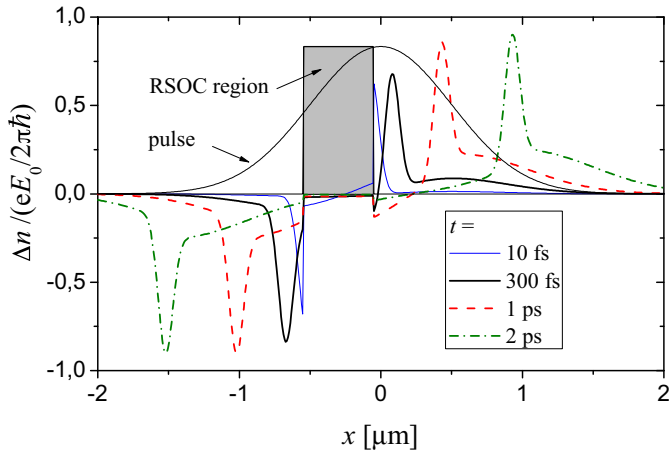
Fig. 3. The photoexcitation process induced by a Gaussian electric pulse (39) (thin black solid line) partially overlapping with a RSOC region (grey area): the profile of the photoexcited densities is plotted as a function of the spatial coordinate x along the QSH edge, at different time snapshots. The parameters of the Gaussian pulse (39) are $\Delta = 500\,\text{nm}$ and $\tau = 0.1\,\text{ps}$. The inhomogeneous Fermi velocity (65) induced by the RSOC leads to a fuzzy shape of the wavepackets, resulting from a combination of the photoexcitation inside and outside the RSOC region, where electrons have different Fermi velocities. The RSOC can thus be exploited to tailor the shape of photoexcited wavepackets.

by a time-dependent gate voltage $\mathcal{V}(t)$. Note that the pure photoexcitation process does not involve any electron tunneling from the finger electrodes, differently from the case of electron pumps [2,4,7,10,14,15,83]. The recent advances in pump-probe experiments and photo-current spectroscopy [6,11,47,84–89], make the time-resolved detection of the photoexcited wave packets realistically accessible nowadays.

7 Conclusions

In conclusion, we have shown that, while in the customary far field regime vertical electric dipole transitions are forbidden in QSH edge states, an electric pulse localised in space and/or time and applied at the edge of a QSH system can photoexcite electron wavepackets by intra-branch electrical transitions, without invoking the bulk states or the Zeeman coupling. Several interesting features are found. First, the wavepackets are spin-polarised and propagate in opposite directions. Their density profile depends linearly on the amplitude of the electric pulse, is independent of the initial equilibrium temperature and does not disperse during propagation [see Fig. 1]. This result, quite different from the one obtained in usual Schrödinger systems described by a parabolic spectrum, is exact and does not rely on any linear response approximation. It is due to the linearity of the spectrum. Secondly, we have analyzed the energy correlations and in particular the photoinduced energy distribution. We have shown that such quantity does depend on temperature and on the amplitude of the applied pulse in a highly non-linear way [see Fig. 2]. Furthermore in energy domain the photoexcitation process does not merely amount to a redistribution of states from below to above the Fermi level, rather it also involves a net creation of charge on one branch (compensated by the annihiliation on the other branch). This effect, which is the gist of the chiral anomaly characterizing massless

Dirac electrons, is particularly evident in the case of a Lorentzian pulse with amplitude parameter $u_0 = 1$ [see Fig. 2b] that describes minimal particle excitations known as Levitons [38–40]. These results may pave the way to the observation of Levitons in QSH, whose existence has been so far experimentally proven in ballistic channels in 2DEG [47–50]. Also, we have discussed the effects of Rashba spin–orbit coupling on the photoexcitation process, showing that the former can be exploited to tailor the shape of photoexcited wavepackets [see Fig. 3]. Finally, we have proposed possible experimental realizations. These results support the idea that QSH edge states might be successfully exploited in the near future as a promising alternative platform for electron quantum optics [27–33], which is nowadays mostly limited to quantum Hall systems [4–15] with the unavoidable drawback of the strong magnetic fields. In contrast, time-reversal topological insulators, which are based on spin–orbit coupling, are immune to such drawback and offer the additional possibility of generating spin-polarised electron wave packets.

Author contribution statement

The authors contributed equally to this manuscript.

References

1. A. Bertoni, P. Bordone, R. Brunetti, C. Jacoboni, S. Reggiani, Phys. Rev. Lett. **84**, 5912 (2000)
2. M.D. Blumenthal, B. Kaestner, L. Li, S. Giblin, T.J. B.M. Janssen, M. Pepper, D. Anderson, G. Jones, D.A. Ritchie, Nat. Phys. **3**, 343 (2007)
3. E. Bocquillon, F.D. Parmentier, C. Grenier, J.-M. Berroir, P. Degiovanni, B. Plaçais, A. Cavanna, Y. Jin, G.Fève, Phys. Rev. Lett. **108**, 196803 (2012)
4. G. Fève, A. Mahé, J.-M. Berroir, T. Kontos, B. Plaçais, D.C. Glattli, A. Cavanna, B. Etienne, Y. Jin, Science **316**, 1169 (2007)
5. P. Roulleau, F. Portier, P. Roche, A. Cavanna, G. Faini, U. Gennser, D. Mailly, Phys. Rev. Lett. **100**, 126802 (2008)
6. A. Mahé, F.D. Parmentier, E. Bocquillon, J.-M. Berroir, D.C. Glattli, T. Kontos, B. Plaçais, G. Fève, A. Cavanna, Y. Jin, Phys. Rev. B **82**, 201309(R) (2010)
7. Ch. Grenier, R. Hervé, E. Bocquillon, F.D. Parmentier, B. Plaçais, J.M. Berroir, G. Fève, P. Degiovanni, New J. Phys. **13**, 093007 (2011)
8. E. Bocquillon, V. Freulon, J.-M. Berroir, P. Degiovanni, B. Plaçais, A. Cavanna, Y. Jin, G. Fève, Nat. Commun. **4**, 1839 (2013)
9. E. Bocquillon, V. Freulon, J.-M Berroir, P. Degiovanni, B. Plaçais, A. Cavanna, Y. Jin, G. Fève, Science **339**, 1054 (2013)
10. J.D. Fletcher, P. See, H. Howe, M. Pepper, S.P. Giblin, J.P. Griffiths, G.A.C. Jones, I. Farrer, D.A. Ritchie, T.J.B. M. Janssen, M. Kataoka, Phys. Rev. Lett. **111**, 216807 (2013)
11. E. Bocquillon, V. Freulon, F.D. Parmentier, J.-M Berroir, B. Plaçais, C. Wahl, J. Rech, T. Jonckheere, T. Martin, C. Grenier, D. Ferraro, P. Degiovanni, G. Fève, Ann. Phys. (Berlin) **526**, 1 (2014)
12. C. Wahl, J. Rech, T. Jonckheere, T. Martin, Phys. Rev. Lett. **112**, 046802 (2014)
13. V. Freulon, A. Marguerite, J.-M. Berroir, B. Plaçais, A. Cavanna, Y. Jin, and G. Fève, Nature Commun. **6**, 6854 (2015)
14. J. Waldie, P. See, V. Kashcheyevs, J.P. Griffiths, I. Farrer, G.A.C. Jones, D.A. Ritchie, T.J.B.M. Janssen, M. Kataoka, Phys. Rev. B **92**, 125305 (2015)

15. M. Kataoka, N. Johnson, C. Emary, P. See, J.P. Griffiths, G.A.C. Jones, I. Farrer, D.A. Ritchie, M. Pepper, T.J.B.M. Janssen, Phys. Rev. Lett. **116**, 126803 (2016)
16. C. L. Kane, E. J. Mele, Phys. Rev. Lett. **95**, 146802 (2005)
17. C. L. Kane, E. J. Mele, Phys. Rev. Lett. **95**, 226801 (2005)
18. B.A. Bernevig, T.L. Hughes, S.-C. Zhang, Science **314**, 1757 (2006)
19. M.König, S. Wiedmann, C. Brüne, A. Roth, H. Buhmann, L.W. Molenkamp, X.-L. Qi, S.-C. Zhang, Science **318**, 766 (2006)
20. M.König, H. Buhmann, L W. Molenkamp, T.L. Hughes, C.-X. Liu, X.-L. Qi, S.-C. Zhang, J. Phys. Soc. Jpn. **77**, 031007 (2008)
21. A. Roth, C. Brüne, H. Buhmann, L.W. Molenkamp, J. Maciejko, X.-L. Qi, S.-C. Zhang, Science **325**, 294 (2009)
22. C. Brüne, A. Roth, H. Buhmann, E.M. Hankiewicz, L. W. Molenkamp, J. Maciejko, X.-L. Qi, S.-C. Zhang, Nat. Phys. **8**, 485 (2012)
23. C. Liu, T.L. Hughes, X.-L. Qi, K. Wang, S.-C. Zhang, Phys. Rev. Lett. **100**, 236601 (2008)
24. I. Knez, R.-R. Du, G. Sullivan, Phys. Rev. Lett. **107**, 136603 (2011)
25. I. Knez, C.T. Rettner, S.-H. Yang, S.S.P. Parkin, L. Du, R.-R. Du, G. Sullivan, Phys. Rev. Lett. **112**, 026602 (2014)
26. E.M. Spanton, K.C. Nowack, L. Du, G. Sullivan, R.-R. Du, K.A. Moler, Phys. Rev. Lett. **113**, 026804 (2014)
27. A. Inhofer, D. Bercioux, Phys. Rev. B **88**, 235412 (2013)
28. P.P. Hofer, M.Büttiker, Phys. Rev. B **88**, 241308 (2013)
29. D. Ferraro, C. Wahl, J. Rech, T. Jonckheere, T. Martin, Phys. Rev. B **89**, 075407 (2014)
30. A. Ström, H. Johannesson, P. Recher, Phys. Rev. B **91**, 245406 (2015)
31. A. Calzona, M. Acciai, M. Carrega, F. Cavaliere, M. Sassetti, Phys. Rev. B **94**, 035404 (2016)
32. F. Dolcini, R.C. Iotti, A. Montorsi, F. Rossi, Phys. Rev. B **94**, 165412 (2016)
33. F. Dolcini, Phys. Rev. B **95**, 085434 (2017)
34. B. Dóra, J. Cayssol, F. Simon, R. Moessner, Phys. Rev. Lett. **108**, 056602 (2012)
35. S.N. Artemenko, V.O. Kaladzhyan, JETP Lett. **97**, 82 (2013)
36. G. Dolcetto, F. Cavaliere, M. Sassetti, Phys. Rev. B **89**, 125419 (2014)
37. V. Kaladzhyan, P.P. Aseev, S.N. Artemenko, Phys. Rev. B **92**, 155424 (2015)
38. L.S. Levitov, H. Lee, G.B. Lesovik, J. Math. Phys. **37**, 4845 (1996)
39. D.A. Ivanov, H.W. Lee, L.S. Levitov, Phys. Rev. B **56**, 6839 (1997)
40. J. Keeling, I. Klich, L.S. Levitov, Phys. Rev. Lett. **97**, 116403 (2006)
41. M. Moskalets, Phys. Rev. B **89**, 045402 (2014)
42. D. Dasenbrook, C. Flindt, Phys. Rev. B **92**, 161412 (2015)
43. M. Moskalets, Phys. Rev. Lett. **117**, 046801 (2016)
44. M. Moskalets, Low Temp. Phys. **43**, 865 (2017)
45. J. Rech, D. Ferraro, T. Jonckheere, L. Vannucci, M. Sassetti, T. Martin, Phys. Rev. Lett. **118**, 076801 (2017)
46. L. Vannucci, F. Ronetti, J. Rech, D. Ferraro, T. Jonckheere, T. Martin, M. Sassetti, Phys. Rev. B **95**, 245415 (2017)
47. J. Dubois, T. Jullien, F. Portier, P. Roche, A. Cavanna, Y. Jin, W. Wegscheider, P. Roulleau, D.C. Glattli, Nature **502**, 659 (2013)
48. J. Dubois, T. Jullien, C. Grenier, P. Degiovanni, P. Roulleau, D.C. Glattli, Phys. Rev. B **88**, 085301 (2013)
49. T. Jullien, P. Roulleau, B. Roche, A. Cavanna, Y. Jin, D.C. Glattli, Nature **514**, 603 (2014)
50. D.C. Glattli, P.S. Roulleau, Phys. Status Sol. **254**, 1600650 (2017)
51. S.L. Adler, Phys. Rev. **177**, 2426 (1969)
52. J.S. Bell, R. Jackiw, Nuovo Cim. **A 60**, 47 (1969)
53. H.B. Nielsen, N. Ninomiya, Phys. Lett. **B130**, 389 (1983)
54. R.A. Bertlmann, *Anomalies in quantum field theory* (Clarendon Press, Oxford, 1996)
55. A.A. Zyuzin, A.A. Burkov, Phys. Rev. B **86**, 115133 (2012)

56. H.-J. Kim, K.-S. Kim, J.-F. Wang, M. Sasaki, N. Satoh, A. Ohnishi, M. Kitaura, M. Yang, L. Li, Phys. Rev. Lett **111**, 246603 (2013)
57. S.A. Parameswaran, T. Grover, D.A. Abanin, D.A. Pesin, A. Vishwanath, Phys. Rev. X **4**, 031035 (2014)
58. Y. Takane, J. Phys. Soc. Jpn **85**, 013706 (2016)
59. Z.K. Liu, B. Zhou, Y. Zhang, Z.J. Wang, H.M. Weng, D. Prabhakaran, S.-K. Mo, Z.X. Shen, Z. Fang, X. Dai, Z. Hussain, Y.L. Chen, Science **343**, 864 (2014)
60. S.-Y. Xu, I. Belopolski, N. Alidoust, M. Neupane, G. Bian, C. Zhang, R. Sankar, G. Chang, Z. Yuan, C.-C. Lee, S.-M. Huang, H. Zheng, J. Ma, D.S. Sanchez, B.Wang, A. Bansil, F. Chou, P.P. Shibayev, H. Lin, S. Jia, M.Z. Hasan, Science **349**, 613 (2015)
61. S.-Y. Xu, I. Belopolski, D.S. Sanchez, C. Zhang, G. Chang, C. Guo, G. Bian, Z. Yuan, H. Lu, T.-R. Chang, P.P. Shibayev, M.L. Prokopovych, N. Alidoust, H. Zheng, C.-C. Lee, S.-M. Huang, R. Sankar, F. Chou, C.-H. Hsu, H.-T. Jeng, A. Bansil, T. Neupert, V.N. Strocov, H. Lin, S. Jia, M.Z. Hasan, Science **349**, 622 (2015)
62. J. Xiong, S.K. Kushwaha, T. Liang, J.W. Krizan, M. Hirschberger, W. Wang, R.J. Cava, N.P. Ong, Science **350**, 413 (2015)
63. C. Fleckenstein, N. Traverso Ziani, B. Trauzettel, Phys. Rev. B **94**, 241406(R) (2016)
64. R. Rosati, F. Dolcini, F. Rossi, Appl. Phys. Lett. **106**, 243101 (2015)
65. Ch. Grenier, J. Dubois, T. Jullien, P. Roulleau, D.C. Glattli, P. Degiovanni, Phys. Rev. B **88**, 085302 (2013)
66. E.Ya. Sherman, Phys. Rev. B **67**, 161303 (2003)
67. E.Ya. Sherman, Appl. Phys. Lett. **82**, 209 (2003)
68. M.V. Entin, L.I. Magarill, Phys. Rev. B **64**, 085330 (2001)
69. J.I.Väyrynen, T. Ojanen, Phys. Rev. Lett. **106**, 076803 (2011)
70. C. Ortix, Phys. Rev. B **91**, 245412 (2015)
71. P. Gentile, M. Cuoco, C. Ortix, Phys. Rev. Lett. **115**, 256801 (2015)
72. Z.-J. Ying, P. Gentile, C. Ortix, M. Cuoco, Phys. Rev. B **94**, 081406(R) (2016)
73. J. Hinz, H. Buhmann, M. Schäfer, V. Hock, C.R. Becker, L.W. Molenkamp, Semi. Sci. Tech. **21**, 501 (2006)
74. Z. Qiao, X. Li, W.K. Tse, H. Jiang, Y. Yao, Q. Niu, Phys. Rev. B **87**, 125405 (2013)
75. Y.H. Park, S.-H. Shin, J.D. Song, J. Chang, S.H. Han, H.-J. Choi, H.C. Koo, Solid-State Electron. **82**, 23 (2013)
76. P. Wójcik, J. Adamowski, B.J. Spisak, M. Wołoszyn, J. Appl. Phys. **115**, 104310 (2014)
77. L. Novotny, S.J. Stranick, Ann. Rev. Phys. Chem. **57**, 303 (2006)
78. B. Hanewinkel, A. Knorr, P. Thomas, S.W. Koch, Phys. Rev. B **55**, 13715 (1997)
79. A. Hartschuh, E.J. Sánchez, X.S. Xie, L. Novotny, Phys. Rev. Lett. **90**, 095503 (2003)
80. H. Ito, K. Furuya, Y. Shibata, S. Kashiwaya, M. Yamaguchi, T. Akazaki, H. Tamura, Y. Ootuka, S. Nomura, Phys. Rev. Lett. **107**, 256803 (2011)
81. S. Mamyouda, H. Ito, Y. Shibata, S. Kashiwaya, M. Yamaguchi, T. Akazaki, H. Tamura, Y. Ootuka, S. Nomura, Nanolett. **15**, 4127 (2015)
82. F. Dolcini, Phys. Rev. B **85**, 033306 (2012)
83. M. Acciai, A. Calzona, G. Dolcetto, T.L. Schmidt, M. Sassetti, Phys. Rev. B **96**, 075144 (2017)
84. C. Altimiras, H. le Sueur, U. Gennser, A. Cavanna, D. Mailly, F. Pierre, Nat. Phys. **6**, 34 (2009)
85. A. Brenneis, L. Gaudreau, M. Seifert, H. Karl, M.S. Brandt, H. Huebl, J.A. Garrido, F.H.L. Koppens, A.W. Holleitner, Nat. Nanotech. **10**, 135 (2014)
86. H. Kamata, N. Kumada, M. Hashisaka, K. Muraki, T. Fujisawa, Nat. Nanotech. **9**, 177 (2014)
87. C. Kastl, C. Karnetzky, H. Karl, A.W. Holleitner, Nature Commun. **6**, 6617 (2015)
88. A. Woessner, P. Alonso-González, M.B. Lundeberg, Y. Gao, J.E. Barrios-Vargas, G. Navickaite, Q. Ma, D. Janner, K. Watanabe, A.W. Cummings, T. Taniguchi, V. Pruneri, S. Roche, P. Jarillo-Herrero, J. Hone, R. Hillenbrand, F.H.L. Koppens, Nat. Commun. **7**, 10783 (2016)
89. M. Hashisaka, N. Hiyama, T. Akiho, K. Muraki, T. Fujisawa, Nat. Phys. **13**, 559 (2017)